

Reducing lattice thermal conductivity via phonon engineering: Strategies for high-performance thermoelectrics

Yayu Wang(王亚雨), Hou Jue(侯爵), Ming Yang(杨明), and Xingli Zhang(张兴丽)
Citation: Chin. Phys. B, 2026, 35 (**3**): 037201. DOI: 10.1088/1674-1056/ae1c22
http://cpb.iphy.ac.cn; http://iopscience.iop.org/cpb

What follows is a list of articles you may be interested in

Realize high thermoelectric performance in both zone-melted ingots and powder-metallurgy bulks of $Bi_{0.46}Sb_{1.54}Te_3$

Kai-Wen Zhao(赵凯雯), Meng-Yao Li(李梦瑶), Ying-Jiu Zhang(张迎九), and Hong-Zhang Song(宋红章)
Chin. Phys. B, 2025, 34 (**10**): 107203. DOI: 10.1088/1674-1056/add503

High thermoelectric performance of SnS under high pressure and high temperature

Yuqi Gao(高语崎), Xinglin Wang(王星淋), Cun You(由存), Dianzhen Wang(王殿振), Nan Gao(高楠), Qi Jia(贾琪), Zhihui Li(李志慧), Qiang Tao(陶强), and Pinwen Zhu(朱品文)
Chin. Phys. B, 2025, 34 (**8**): 087201. DOI: 10.1088/1674-1056/addbc8

High-entropy alloys in thermoelectric application: A selective review

Kai Ren(任凯), Wenyi Huo(霍文燚), Shuai Chen(陈帅), Yuan Cheng(程渊), Biao Wang(王彪), and Gang Zhang(张刚)
Chin. Phys. B, 2024, 33 (**5**): 057202. DOI: 10.1088/1674-1056/ad34c5

Ga intercalation in van der Waals layers for advancing p-type Bi_2Te_3-based thermoelectrics

Yiyuan Chen(陈艺源), Qing Shi(石青), Yan Zhong(钟艳), Ruiheng Li(李瑞恒), Liwei Lin(林黎蔚), Ding Ren(任丁), Bo Liu(刘波), and Ran Ang(昂然)
Chin. Phys. B, 2023, 32 (**6**): 067201. DOI: 10.1088/1674-1056/acc2af

Advancing thermoelectrics by suppressing deep-level defects in Pb-doped $AgCrSe_2$ alloys

Yadong Wang(王亚东), Fujie Zhang(张富界), Xuri Rao(饶旭日), Haoran Feng(冯皓然), Liwei Lin(林黎蔚), Ding Ren(任丁), Bo Liu(刘波), and Ran Ang(昂然)
Chin. Phys. B, 2023, 32 (**4**): 047202. DOI: 10.1088/1674-1056/acb765

TOPICAL REVIEW — Heat conduction and its related interdisciplinary areas

Reducing lattice thermal conductivity via phonon engineering: Strategies for high-performance thermoelectrics

Yayu Wang(王亚雨)[1,2], Jue Hou(侯爵)[1], Ming Yang(杨明)[2,†], and Xingli Zhang(张兴丽)[1,‡]

[1] *College of Mechanical and Electrical Engineering, Northeast Forestry University, Harbin* 150040, *China*
[2] *Institute of Engineering Thermophysics, Chinese Academy of Sciences, Beijing* 100190, *China*

(Received 3 September 2025; revised manuscript received 21 October 2025; accepted manuscript online 6 November 2025)

Thermoelectric materials convert heat directly into electricity and are therefore promising for energy harvesting and environmental applications. Ideal high-performance thermoelectrics combine ultralow lattice thermal conductivity, κ_L, with high carrier mobility, a paradigm commonly termed phonon-glass electron-crystal. However, strong coupling between electronic and phononic transport complicates simultaneous optimization of these properties. Because κ_L is largely independent of electronic transport, targeted suppression of κ_L is an effective route to partially decouple heat and charge transport. This review summarizes recent advances in reducing κ_L via two complementary approaches: phonon engineering of bulk nanostructured systems and phonon engineering of low-dimensional materials. In bulk systems, κ_L may be minimized while retaining high electrical conductivity and maximizing the thermoelectric figure of merit ZT by controlling three fundamental phonon parameters: the volumetric specific heat c_v, the phonon group velocity v_g, and the phonon relaxation time τ. Low-dimensional architectures, including superlattices, nanowires, and nanocomposites, supply additional levers to suppress lattice heat transport and to tailor the electronic structure. Integrating multiscale and multimodal phonon-control strategies enables significant reductions in κ_L without sacrificing electronic performance, thereby advancing the phonon-glass electron-crystal paradigm.

Keywords: thermoelectric materials, lattice thermal conductivity, phonon engineering, bulk nanostructures, low-dimensional structures

PACS: 72.15.Jf, 63.20.kg, 84.60.Rb, 73.21.–b

DOI: 10.1088/1674-1056/ae1c22 **CSTR:** 32038.14.CPB.ae1c22

1. Introduction

The accelerating global shortage of resources and mounting environmental concerns are creating an urgent need for sustainable clean-energy technologies. Thermoelectric materials and devices — which contain no moving parts — can directly convert heat into electricity via the Seebeck effect (Fig. 1),[1] or convert electrical energy into heating or cooling via the Peltier effect (Fig. 1).[1] Consequently, thermoelectric devices can harvest thermal energy from sources such as solar heat and industrial waste heat, thereby improving overall resource-use efficiency. Owing to these attributes, thermoelectrics have attracted considerable interest and found applications in industrial waste-heat recovery,[2] power generation from natural heat sources,[3] wearable thermal energy systems,[4] automotive waste-heat recovery,[5] thermoelectric refrigeration,[6] microprocessor cooling, and cooling of medical devices.[7,8] They are therefore considered promising solutions to energy supply and environmental challenges.

The performance of a thermoelectric material is quantified by the dimensionless figure of merit ZT,[9] defined as $ZT = TS^2\sigma/k$, where T is the temperature, S is the Seebeck coefficient, σ is the electrical conductivity, and κ is mainly composed of the electronic and lattice thermal conductivities (κ_e and κ_L).[10] High ZT requires a large power factor ($S^2\sigma$) combined with low κ; however, S, σ and κ are mutually interdependent, so improving one quantity typically perturbs

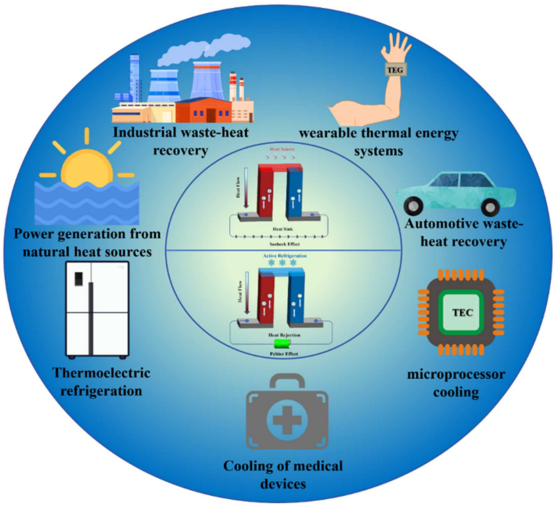


Fig. 1. Introduction of thermoelectric effects and summary of thermoelectric applications of materials. The schematic illustrates thermoelectric effects, including the Seebeck effect related to power generation and the Peltier effect related to cooling.

†Corresponding author. E-mail: yangming@iet.cn
‡Corresponding author. E-mail: zhang-xingli@nefu.edu.cn

© 2026 Chinese Physical Society and IOP Publishing Ltd. All rights, including for text and data mining, AI training, and similar technologies, are reserved.

the others. In particular, S and σ vary inversely with carrier concentration n, producing a fundamental trade-off in device optimization.[11] Thus, strategies that partially decouple electronic and phononic transport are essential to increase ZT.

Among the transport coefficients, the lattice thermal conductivity κ_L is relatively independent and critically important for thermoelectric performance;[12,13] reducing κ_L often yields the largest practical gains in ZT.[14–16] From kinetic theory, κ_L depends on the phonon volumetric specific heat c_v, the phonon group velocity v_g, and the phonon relaxation time τ.[14] Accordingly, three principal routes exist to reduce κ_L: (i) shorten τ tuned by defect engineering (e.g., zero-dimensional point defects,[17–19] one-dimensional dislocations,[20–22] and two-dimensional interfaces such as grain boundaries, nanotwins, and stacking faults[23–26]), (ii) reduce v_g via lattice softening or heavy-atom substitution,[27–29] and (iii) lower c_v (for example, via superionic behavior[30]). Although these strategies have been demonstrated effectively in three-dimensional materials, a key limitation remains: the inverse relationship between S and σ with carrier concentration constrains further increases in ZT.[31] In the late 1990s Hicks and Dresselhaus[32] proposed that reduced dimensionality can increase the electronic density of states near the Fermi level, thereby enhancing S, while surface and interface scattering can preferentially suppress phonon transport with limited degradation of σ.[33–35] This insight motivates two complementary nanoscale paradigms for improving thermoelectric performance: the phonon engineering of bulk nanostructured materials and the phonon engineering of low-dimensional nanomaterials.

This review summarizes recent progress in suppressing the κ_L of thermoelectric materials, with emphasis on two complementary approaches: phonon engineering of bulk nanostructured systems and phonon engineering of low-dimensional nanomaterials. In bulk systems, κ_L may be minimized while preserving high electrical conductivity and maximizing the thermoelectric figure of merit ZT by tuning three primary phonon parameters: the volumetric specific heat c_v, the phonon group velocity v_g and the phonon relaxation time τ. We then examine how low-dimensional architectures, including superlattices, nanowires and nanocomposites, further reduce lattice heat transport and thereby enhance thermoelectric performance. Finally, we highlight remaining challenges and opportunities for translating these strategies into practical, scalable thermoelectric devices.

2. Phonon engineering for bulk nanostructured materials

2.1. Defect engineering

Phonon relaxation time τ can be tuned by introducing scattering centers of different dimensionalities, including zero-dimensional (0D) point defects, one-dimensional (1D) line defects, and two-dimensional (2D) planar defects.

2.1.1. Point defects

Point defects are atomic-scale lattice perturbations, typically classified as vacancies, substitutional impurities, or interstitials. They influence electronic transport by altering the carrier concentration (e.g., the Hall carrier concentration n_H) and efficiently scatter short-wavelength phonons via local mass and force-constant disorder, thereby reducing the lattice thermal conductivity.[36] The effect of point defects on phonon relaxation can be described within the Debye–Callaway framework,[37] in which the defect-induced phonon scattering rate often follows a Rayleigh-type frequency dependence (approximately $\propto \omega^4$) for small defects.[38] For substituted elements (point defects), the associated phonon scattering rate is often written as $\tau_p^{-1} = \frac{V\omega^4}{4\pi v^3}\Gamma$,[17] where Γ is the scattering parameter. According to the models of Slack and Abeles,[39,40] Γ can be decomposed into mass-fluctuation and strain-field contributions, $\Gamma = \Gamma_M + \Gamma_S$, where Γ_M accounts for mass disorder (mass contrast between host and substituent atoms) and Γ_S describes scattering due to local strain/force-constant perturbations. These terms can be evaluated from the defect concentrations and the corresponding mass and size/elastic mismatches. Therefore, the strong mass fluctuation and strain-field fluctuation induced by point defects can significantly reduce κ_L.[41]

In the Cu_2SnSe_3 system (Fig. 2(a)),[17] partial substitution of Cu by different dopants produces markedly different effects on the lattice thermal conductivity κ_L. Replacing 10% of Cu with Ni or Zn yields only a negligible change in κ_L, whereas 10% substitution by heavier or more size-mismatched elements such as Cd, Ag, or Al causes a pronounced reduction in κ_L. This behavior is primarily attributable to stronger mass-fluctuation and strain-field scattering induced by the latter dopants. Figure 2(b) shows that introducing extrinsic defects (Cd, Ga, In, Mn, Ge, Zn, and Al) systematically suppresses κ_L across the entire measured temperature range; notably, substituting 10% of Sn with Al reduces κ_L by $\sim 71.5\%$ at 300 K and by $\sim 50.9\%$ at 850 K.[17] Wang *et al.*[18] experimentally demonstrated that Pb incorporation into cubic SnSe synergistically improves thermoelectric transport by concurrently increasing the hole concentration and reducing the lattice thermal conductivity κ_L. At a Pb content of $x = 0.08$, the peak power factor at 300 K increases to 20 $\mu W \cdot cm^{-1} \cdot K^{-2}$. The atomic-size mismatch introduced by Pb generates enhanced internal microstrain, which elevates phonon scattering and lowers κ_L; with increasing Pb concentration, lattice-distortion (strain) fluctuations intensify, further promoting phonon attenuation. These local bonding inhomogeneities and the associated increase in lattice anharmonic-

ity therefore produce additional reductions in κ_L. A complementary and increasingly adopted strategy to suppress κ_L is targeted doping with atoms that possess stereochemically active lone-pair s electrons, which induce local bonding disorder and amplify lattice anharmonicity.[43] Although compounds that intrinsically contain active lone pairs are scarce, intentional incorporation of lone-pair dopants can create localized low-frequency vibrational modes and severe local distortions, yielding phonon scattering that far exceeds predictions from simple mass-fluctuation or point-defect models. The effectiveness of this "anharmonic-atom" doping mechanism has been demonstrated in $CuFeS_2$ chalcopyrite. Substitution of Cu by In (which carries stereochemically active lone pairs) distorts the local coordination away from ideal tetrahedral symmetry (Fig. 2(c)) and induces localized low-frequency modes that couple strongly to the host phonon spectrum, thereby substantially increasing lattice anharmonicity. As shown in Fig. 2(d), only 3 at.% In on the Cu site reduces κ_L by $> 40\%$.[42] A comparable phenomenon occurs in Bi-doped GeTe, where 10 at.% Bi yields $\sim 37\%$ reduction in κ_L at 740 K, an effect attributed to the strong anharmonicity introduced by Bi lone-pair cations.[42]

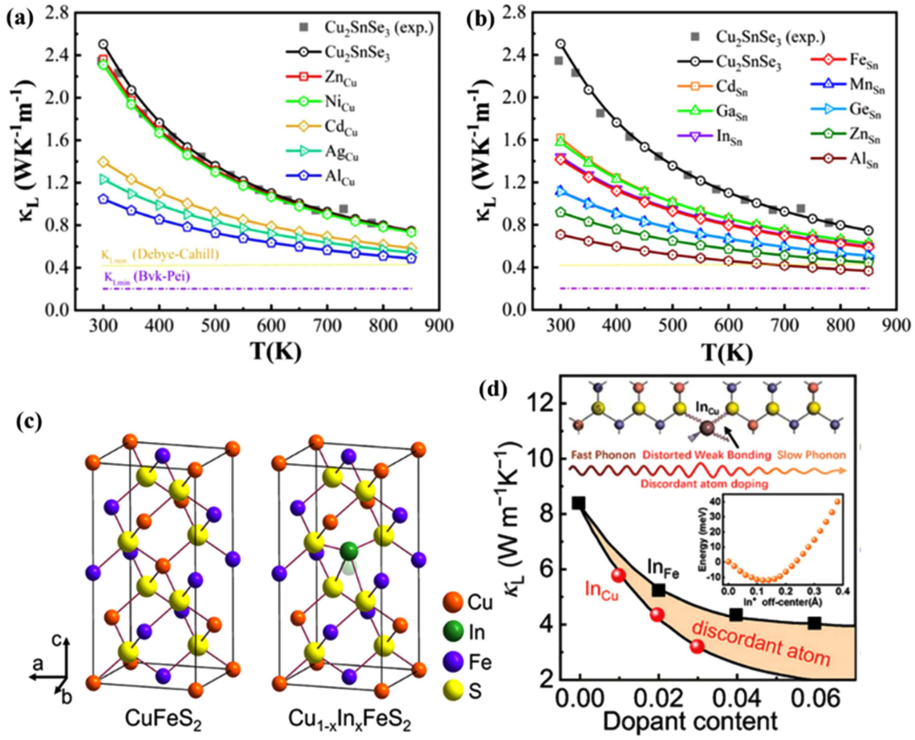


Fig. 2. (a) Calculated lattice thermal conductivity of Cu_2SnSe_3 with substituting 10% Cu by Zn, Ni, Cd, Ag, and Al. Reproduced with permission from Ref. [17]. (b) Calculated lattice thermal conductivity of Cu_2SnSe_3 with substituting 10% Sn by Cd, Ga, In, Fe, Mn, Ge, Zn, and Al. Reproduced with permission from Ref. [17]. (c) Crystal structure of $CuFeS_2$ and $Cu_{1-x}In_xFeS_2$. The left one is the perfect crystal structure of $CuFeS_2$. The right structure illuminates when the discordant In^+ substitutes on the Cu sublattice, the lone pair electron of In^+ is incompatible with the tetrahedral geometry of the chalcopyrite sites, which results in the off-center behavior of In^+. Reproduced with permission from Ref. [42]. (d) Room temperature lattice thermal conductivity of $CuFeS_2$ compounds with different doping concentrations. Reproduced with permission from Ref. [42].

In addition to elemental doping, an appropriate concentration of vacancies can optimize carrier scattering, thereby balancing electrical conductivity σ and the Seebeck coefficient S to improve the power factor $S^2\sigma$.[44,45] Vacancies also introduce additional phonon-scattering centers, shortening phonon mean free paths and slowing heat transport, which effectively reduces the lattice thermal conductivity κ_L. For example, in polycrystalline SnSe, α-radiation–induced intrinsic Sn vacancies enhance phonon scattering and reduce κ_L to 0.22 $W{\cdot}m^{-1}{\cdot}K^{-1}$, yielding a high ZT of 2.4 at 800 K.[19] Similarly, Chen *et al.*[46] obtained an ultralow κ_L of 0.4 $W{\cdot}m^{-1}{\cdot}K^{-1}$ in a SnTe–$AgSbTe_2$ alloy by increasing the vacancy concentration, underscoring the important role of vacancy defects in enhancing thermoelectric performance.

Various point-defect engineering strategies have been developed to suppress the κ_L of thermoelectric materials. In addition to conventional elemental doping and vacancy engineering, high-entropy design, in which multiple distinct elements share a single crystallographic sublattice, has emerged as an effective and widely adopted strategy.[47,48] Entropy engineering acts via two synergistic mechanisms: (1) entropy-driven structural stabilization, which can preserve or even enhance electronic transport by stabilizing higher-symmetry single-phase structures and promoting band convergence; and (2) severe lattice distortion and chemical/force-constant disorder, which induce strong mass- and strain-field fluctuations that generate dense, multiscale phonon scattering and dramatically reduce κ_L.[49] These combined effects enable high-entropy compounds to achieve unusually low lattice thermal conductivities while retaining favorable electronic properties

(e.g., long-range carrier transport in an ordered lattice coexisting with atom-scale disorder). Thermodynamically, the high-entropy effect is rooted in the Gibbs free-energy relation $\Delta G = \Delta H - T\Delta S < 0$, where ΔH, T and ΔS denote the enthalpy change, absolute temperature, and configurational entropy change, respectively.[50]

Increasing configurational entropy lowers ΔG and can therefore stabilize single-phase (often high-symmetry) structures over multiphase mixtures, as illustrated schematically in Fig. 3(a).[50] The absence of secondary-phase interfaces reduces carrier scattering at phase boundaries and — when combined with enhanced band degeneracy in the stabilized phase — supports excellent electronic transport. Concurrently, the severe lattice-distortion effect produced by atomic-radius and bonding mismatches increases lattice anharmonicity, preferentially scattering mid- to high-frequency phonons and further suppressing κ_L. Moreover, lattice distortion and chemical disorder can impede long-range defect motion (e.g., dislocation glide), which modifies mechanical behavior and can help sustain the engineered microstructure. Within the complex high-entropy matrix, synergistic interactions among multiple elements therefore enhance both thermoelectric and mechanical properties (Fig. 3(b)).[50]

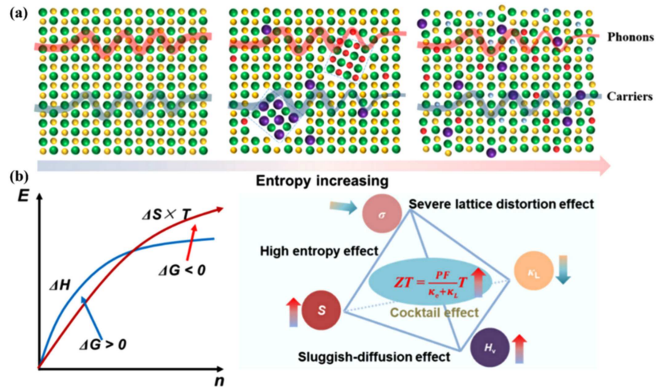


Fig. 3. Synergistic optimization of thermoelectric and mechanical properties via high-entropy engineering. (a) Schematic of carrier and phonon transport in a high-entropy matrix with pronounced lattice distortion. Reproduced with permission from Ref. [50]. (b) Schematic illustration of the Gibbs free-energy landscape versus compositional complexity; the red and blue curves represent configurational entropy (ΔS) and formation enthalpy (ΔH), respectively. Reproduced with permission from Ref. [50]. (c) Influence of four core high-entropy effects on thermoelectric transport parameters and mechanical properties: (i) entropy-stabilized single-phase formation, (ii) enhanced band degeneracy and electronic transport, (iii) severe lattice distortion with mass/force-constant disorder, and (iv) multiscale phonon-scattering centers and defect-mediated mechanical strengthening. Reproduced with permission from Ref. [50].

A representative example is GeTe-based high-entropy alloys and compounds. The band structure of cubic GeTe is analogous to those of PbTe and SnTe: the valence-band maximum (VBM) and conduction-band minimum (CBM) occur at the L point of the Brillouin zone (fourfold valley degeneracy, $N_v = 4$), yielding a direct band gap at L. However, a secondary valence band along the Σ direction lies close in energy to the L band; this Σ band has a high nominal degeneracy ($N_v = 12$) and in cubic GeTe the L–Σ energy offset $\Delta E_{L-\Sigma}$ is small (on the order of 60–70 meV).[51,52] Such a small offset facilitates thermal population and band convergence at elevated temperature, providing a route to increase the effective density-of-states mass and thereby to enhance the Seebeck coefficient and power factor. By contrast, the L–Σ offsets reported for PbTe and SnTe are larger ($\sim$ 100 meV and $\sim$ 300 meV, respectively), which renders band convergence less accessible thermally.[53,54] Directional lattice distortion (for example, the rhombohedral distortion along [111]) perturbs the L-point symmetry and shifts the relative energies of the L and Σ bands; in the distorted (rhombohedral) phase the Σ-derived band can become the valence-band maximum, while the L manifold is split by symmetry lowering. Such splitting of valley degeneracies in the low-symmetry phase hinders optimal band convergence and explains why the high-symmetry cubic phase is generally the superior thermoelectric platform at elevated temperatures.[55]

In a representative study (Fig. 4), alloying $LiSbTe_2$ into GeTe was found to stabilize the cubic phase across 300–773 K.[56] During alloying, Li and Sb partially substitute on Ge sites in both the cubic and rhombohedral phases, which suppresses the stereochemical activity of the cation lone pair and lowers the rhombohedral–cubic transition temperature. This stabilization of the cubic phase promotes multiband convergence and enhances phonon scattering, leading to concurrently improved electronic transport and reduced lattice thermal conductivity. Consequently, the alloy attains a high average thermoelectric figure of merit, $ZT_{avg} \approx 1.38$, over the 300–773 K range.[56] Wang *et al.*[56] synthesized single-phase high-entropy alloys in the $Ge_{0.64}Ag_{0.12}Sb_{0.12}X_{0.12}Te$ system (X = Sn, Mn, Pb). Analysis of these GeTe-based samples revealed that local chemical fluctuations are governed by the intrinsic properties of the alloying elements — primarily differences in atomic mass, ionic radius and electronegativity. Beyond increasing configurational entropy via multicomponent alloying, the degree of local structural disorder can be further tuned by varying the elemental composition. Larger elemental mismatch produces enhanced lattice distortions and strain fields, which intensify phonon scattering and substantially suppress the lattice thermal conductivity. Replacing Sn or Mn with Pb enhanced elemental fluctuations and reduced the room-temperature lattice thermal conductivity from ~ 0.88 W·m^{-1}·K^{-1} and ~ 0.73 W·m^{-1}·K^{-1} to ~ 0.61 W·m^{-1}·K^{-1}, respectively — substantially lower than that of pristine GeTe.[57] By tuning the alloy composition to optimize the carrier concentration, the GeTe–AgSbPb composition achieved a peak figure of merit, ZT_{max}, that increased from ~ 1.9 to ~ 2.4, demonstrating the potential of the high-entropy strategy for achieving high-performance thermoelectric materials.[57]

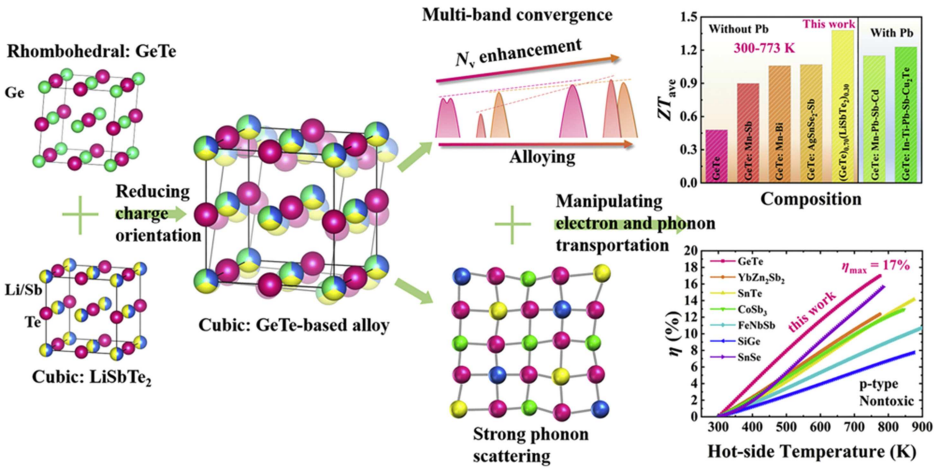


Fig. 4. Schematic demonstration of the origin of crystal structure and the factors responsible for enhanced thermoelectric performance of the GeTe derivatives. Reproduced with permission from Ref. [56].

2.1.2. Linear defects

Point (0D) defects produce Rayleigh-like scattering with a scattering rate proportional to ω^4, and therefore predominantly scatter high-frequency phonons. One-dimensional defects (dislocations) give rise to a scattering rate that scales approximately linearly with frequency, i.e., $\tau_D \sim \omega^{-1}$, and are thus particularly effective at scattering mid-frequency phonons.[58] The role of dislocations in thermoelectric materials — especially their impact on thermal transport — has therefore attracted considerable interest.

The contributions of dislocation cores and of their surrounding strain fields to phonon scattering (Fig. 5) can be expressed phenomenologically as[20,59]

$$\tau_{DC}^{-1} \propto N_D \frac{r^4}{v^2}\omega^3, \tag{1}$$

$$\tau_{DS}^{-1} \propto N_D \frac{\gamma^2 B_D^2 \omega}{2\pi}, \tag{2}$$

where N_D is the dislocation density, r is the effective core radius, B_D the Burgers vector, γ the Grüneisen parameter, ω the phonon angular frequency and v the phonon group velocity. Thus $\tau_{DC} \propto \omega^{-3}$ and $\tau_{DS} \propto \omega^{-1}$, consistent with preferential scattering of mid-frequency phonons by dislocations and of higher-frequency modes by point defects. Such dislocation-mediated scattering efficiently reduces the contribution of mid-frequency phonons to heat transport, thereby lowering the κ_L (Figs. 5(a) and 5(b)).[20] Dislocation-induced reductions in κ_L become substantial when the dislocation density exceeds approximately 10^{12} cm^{-2}.[59,60] Achieving such high densities without degrading electrical transport remains a central challenge. Therefore, dislocation engineering that introduces dense dislocation networks and the associated strain fields provides an effective route to suppress κ_L and improve thermoelectric performance.

In conventional engineering materials, dislocations are typically introduced by plastic deformation to improve mechanical properties.[62] However, most thermoelectric materials are brittle, so conventional deformation rarely generates dislocations.[60] Consequently, dislocations in thermoelectric semiconductors are usually introduced via specialized techniques, for example, interstitial-atom incorporation,[21] vacancy engineering,[22] liquid-phase extrusion,[63] hot deformation,[64] alloying[18] and ultrahigh-pressure sintering.[65]

Interstitial-atom incorporation inserts atoms into lattice interstitial sites, producing local strain that promotes dislocation nucleation. Zhang *et al.*[21] showed that Cu doping in $Pb_{0.9985}Gd_{0.0015}Se$ leads to aggregation of Cu interstitials, nucleation of high-density dislocation networks, and a substantial reduction of κ_L. However, dislocation densities attainable by interstitial or vacancy incorporation alone are constrained by dopant solubility in the host matrix, which makes it difficult to reach ultrahigh densities (e.g., $N_D > 10^{15}$ m^{-2}) in thermoelectric materials. To overcome this limitation, Xu *et al.*[61] developed a two-step strategy. First, heavy Te–S coalloying in a PbSe matrix produces large lattice distortions that increase the driving force for dislocation formation. Second, Cu interstitial doping in the optimized $Pb_{1.02}Se_{0.72}Te_{0.20}S_{0.08}$ composition further accelerates dislocation nucleation. By these successive steps, the $Pb_{1.02}Se_{0.72}Te_{0.20}S_{0.08}$ sample doped with 0.3 at.% Cu attained an ultrahigh dislocation density of 5.4×10^{16} m^{-2}, substantially exceeding previously reported values for n-type PbSe. The dense dislocation network yields ultralow lattice thermal conductivity over the measured temperature range, with κ_L reduced to 0.42 W·m^{-1}·K^{-1} at room temperature and a minimum $\kappa_L \approx 0.29$ W·m^{-1}·K^{-1} at 573 K.[61] Importantly, these dislocations have only a modest effect on carrier transport: the material retains a reasonable weighted mobility and exhibits markedly improved thermoelectric performance, reaching a room-temperature ZT of 0.62 and an average $ZT \approx 0.9$ over 300–573 K. High-angle annular dark-field STEM imaging and strain mapping reveal detailed dislocation structures and their strain fields (HAADF-STEM, GPA and EDS results are presented in Fig. 5).[61] Individual

edge dislocations were directly observed with Burgers vector ($b = 1/2[0\ 1\ 1]$), and geometric phase analysis (GPA) shows pronounced linear strain fields in the ε_{xx} and ε_{yy} components (edge-dislocation image and Burgers circuit: Figs. 5(c) and 5(d); GPA: Figs. 5(e) and 5(f)). Energy-dispersive x-ray spectroscopy (EDS) mapping indicates Cu enrichment near edge dislocations, supporting the role of Cu interstitials in promoting nucleation (Fig. 5(g)). A screw dislocation with Burgers vector ($b = 1/3[1\ 1\ 1]$) was also identified and exhibits strong localized strain fields (HRTEM/HAADF image: Fig. 5(h)). The larger spatial extent of screw-dislocation strain fields (GPA: Figs. 5(i) and 5(j)) likely produces stronger phonon scattering. The contrast between edge- and screw-type strain fields highlights how tailored dislocation architectures can be engineered to suppress lattice heat transport in thermoelectric materials.

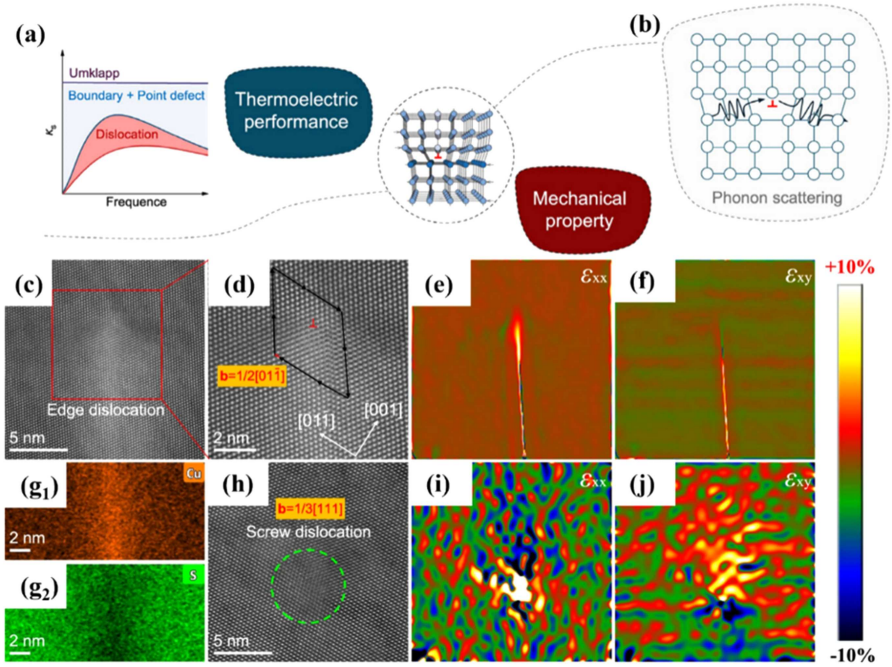


Fig. 5. (a) Thermal conductivity as a function of phonon frequency. Reproduced with permission from Ref. [20]. (b) Schematic of phonon scattering by dislocation cores and associated strain fields. Reproduced with permission from Ref. [20]. (c) HAADF-STEM image of one edge dislocation. Reproduced with permission from Ref. [61]. (d) Burgers vector of the corresponding region of (c). (e), (f) GPA strain analysis of (c). (g_1), (g_2) EDS mapping of Cu and S at edge dislocation. Reproduced with permission from Ref. [61]. (h) HRTEM HADDF image of one screw dislocation. (i), (j) GPA strain analysis of (h). Reproduced with permission from Ref. [61].

In vacancy engineering, intentionally introduced cation vacancies accumulate in the crystal lattice and produce local strain that promotes dislocation nucleation, often during subsequent thermal annealing. Mg_2Sn single crystals grown by melting intrinsically contain Mg vacancies and dislocation cores; both undoped and B-doped specimens therefore show reduced lattice thermal conductivity. For example, undoped crystals prepared by melting display $\kappa_L \approx 4.3$ W·m^{-1}·K^{-1} at 300 K, substantially lower than ~ 7.3 W·m^{-1}·K^{-1} reported for other undoped samples.[66,67] Huang *et al.*[22] further decoupled carrier and phonon transport by B doping, thereby improving thermoelectric performance. Boron increases both the Mg-vacancy concentration and the density of dislocation cores: vacancy clustering and the strain fields induced by doping nucleate dislocations whose cores and surrounding strain fields effectively scatter mid-frequency phonons. Consequently, the lattice thermal conductivity of Mg_2Sn single crystals can be driven toward theoretical minima ($\kappa_{L\,min} \approx 0.65$ W·m^{-1}·K^{-1}).[22]

Liquid-phase extrusion expels excess elements during sintering, inducing lattice stress that promotes dislocation formation. Jung *et al.*[63] synthesized $Bi_{1.7}Sb_{0.3}Te_3$ by transient liquid-phase sintering (LPS) to simultaneously optimize σ and κ_L. Te-rich $Bi_{1.7}Sb_{0.3}Te_3$ ingots were melt-spun into powders with excess Te; these powders undergo LPS at ~ 723 K. Applying external pressure during LPS facilitates the removal of excess Te, causing rapid pellet shrinkage and the formation of dense, interwoven dislocation networks. The resulting interwoven dislocations at grain boundaries strongly scatter phonons, reducing κ_L to 0.4 W·m^{-1}·K^{-1} at 300 K. Concurrently, the Te-rich environment promotes Bi-on-Te antisite formation, which enhances electronic transport and increases σ to 2.2×10^5 S·m^{-1} at 300 K, thereby markedly improving thermoelectric performance.

Hot deformation refers to mechanical processing at elevated temperature (e.g., hot pressing) that enhances ductility and thereby promotes dislocation formation. Chen *et al.*[64] prepared $Bi_{0.5}Sb_{1.5}Te_3$ (BST) polycrystals by zone melting followed by hot deformation. Zone-melted specimens exhibited a well-ordered, defect-free layered microstructure, whereas hot-deformed samples developed dense dislocation networks. These networks strongly scatter mid-frequency

phonons, producing a marked reduction in the κ_L. Geometric phase analysis (GPA) of the ε_{xx} strain component revealed substantial strain fields introduced by the deformation. Such multiscale defect architectures, comprising dislocations and grain boundaries, serve as highly effective phonon-scattering centers and substantially suppress κ_L.

Alloying and doping similarly modify the local coordination environment: atomic-size mismatch between host and dopant induces strain that nucleates dislocations. For example, Wang *et al.*[18] synthesized Pb-doped SnSe by vacuum melting, mechanical activation (MA) and hot-press sintering (HPS). The atomic-size mismatch introduced by Pb generates strain fluctuations that nucleate additional dislocation arrays, thereby enhancing phonon scattering and improving thermal transport.

Ultrahigh-pressure (UHP) sintering produces shear stresses that exceed the threshold for dislocation nucleation in ceramics, thereby enabling extensive dislocation glide and multiplication. Unlike metals and metavalently bonded chalcogenides, ceramic oxides typically resist formation of high-density dislocations under conventional processing owing to strong covalent/ionic bonding and intrinsic brittleness. UHP sintering at gigapascal pressures overcomes this limitation: experiments indicate that GPa-level shear stresses are sufficient to break atomic bonds and nucleate dislocations. Yin *et al.*[65] reported a dislocation density of approximately 9.1×10^{16} m^{-2} in $Bi_{0.96}Pb_{0.04}CuSeO$ ceramics sintered at 2 GPa using UHP processing. Inverse fast-Fourier-transform (IFFT) analysis reveals geometrically necessary dislocations at grain boundaries that produce pronounced ε_{xx} and ε_{xy} strain fields. High-resolution analysis locates edge dislocations with Burgers vector $b = a/2[1\ 1\ 1]$; these dislocations interconnect and coalesce into mesoscale strain domains. The resulting dense dislocation networks strongly suppress phonon transport: the κ_L of BiCuSeO falls to 0.13 $W{\cdot}m^{-1}{\cdot}K^{-1}$ at 767 K, approaching the material's diffusive limit ($\kappa_{diff} \approx 0.07$), while the compound reaches a record thermoelectric figure of merit, $ZT \approx 1.69$ at 767 K, surpassing previously reported BiCuSeO-based materials.[65]

To summarize, effectively introducing dislocations enhances mid-frequency phonon scattering, thereby substantially reducing lattice thermal conductivity (κ_L). By strategically selecting dislocation engineering methods, both thermoelectric and mechanical properties can be optimized, enabling the development of high-performance thermoelectric materials.

2.1.3. Interfacial defects

Interfacial defects are also concerned because of their strong scattering effect on low-frequency phonons ($\tau_{Inter} \sim \omega^0$).[58] The most common two-dimensional (2D) defects (interfacial defects) in thermoelectric materials include grain boundaries, twin boundaries, and stacking faults.[1,68–70]

Grain boundaries, which are the interfaces between grains in polycrystalline materials, play a critical role in phonon scattering.[71] Figure 6(a) shows how thermal conductivity varies with temperature for single-crystal and polycrystalline PbSe.[13,72] While single crystals effectively have infinite grain size, reducing the grain size to the micrometer scale lowers PbSe's lattice thermal conductivity from 4.5 $W{\cdot}m^{-1}{\cdot}K^{-1}$ to approximately 30% of its original value. This reduction arises primarily from the enhanced phonon scattering at grain boundaries.

Grain growth is a diffusion-driven process in which grain boundaries migrate, causing small grains to disappear and large grains to coarsen. Precipitates impede this evolution because lattice mismatch with the matrix raises interfacial energy and thus slows grain-boundary motion. In addition, precipitates trap or scatter mobile species, particularly cations, which reduces the atomic flux into grain interiors and promotes cation-vacancy formation. The consequent reduction in atomic mobility refines the grain-size distribution and stabilizes precipitates at grain boundaries, thereby pinning boundary migration.[73,74]

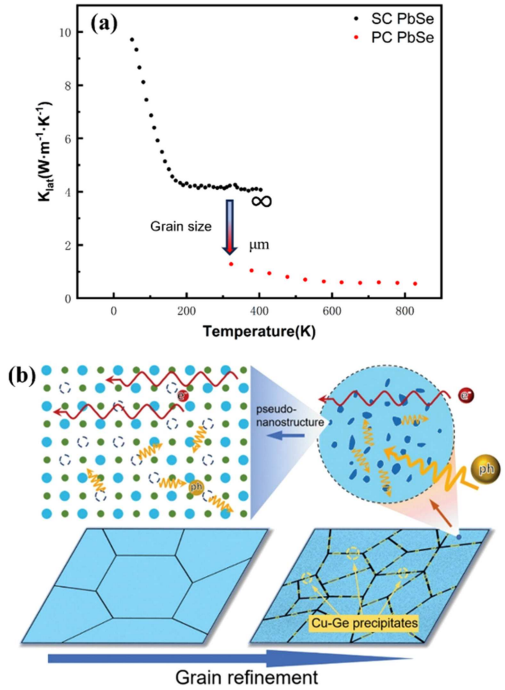


Fig. 6. (a) Comparison of lattice thermal conductivity between single crystalline and polycrystalline PbSe.[13,72] (b) Schematic diagram illustrating grain refinement and pseudo-nanostructures. The pseudo-nanostructures enhance phonon scattering while minimizing the impact on electron transport. Reproduced with permission from Ref. [23].

In n-type $Cu_{0.01}PbSe$, heavy Ge doping drives defect evolution and modifies the electronic structure, markedly improving thermoelectric performance near room temperature. High Ge concentrations induce grain refinement and produce uniformly distributed pseudo-nanostructured vacancy clusters (Fig. 6(b)).[23] These clusters enhance phonon scattering and reduce the lattice thermal conductivity to an ultralow value

of 0.59 $W{\cdot}m^{-1}{\cdot}K^{-1}$ at 300 K. Concurrently, Ge increases the electron effective mass, which compensates for PbSe's intrinsically low Seebeck coefficient and, together with optimized carrier concentration, helps to decouple electronic and phononic transport. Elemental mapping of the n-type $Cu_{0.01}PbSe$ sample shows Ge and Cu enrichment accompanied by Pb depletion. The resulting precipitates further refine the grain structure, increase grain-boundary density, and enhance phonon scattering.[23]

Fu *et al.*[24] similarly introduced sub-microscale grain boundaries into $Fe_{1.05}Nb_{0.75}Ti_{0.25}Sb$ and incorporated abundant atomic-scale point defects to form hierarchical phonon-scattering centers. This architecture reduced the lattice thermal conductivity by $\sim 80\%$ and yielded a peak $ZT \approx 1.34$ at 1150 K. Although mosaic crystals appear single-crystalline at the macroscopic scale, they consist of numerous nanoscale crystallites with varying sizes and orientations and contain abundant low-angle grain boundaries (LAGBs).[75,76] Such microstructures can strengthen thermoelectric performance.[76] To mitigate the trade-off that point defects and other lattice imperfections — while effective at reducing κ_L — often impede electronic transport and reduce carrier mobility, Yang *et al.* introduced dual-site (Ag–Cl) doping in Bi_2S_3 to induce dense LAGBs.[77] This approach simultaneously increased carrier concentration and mobility while suppressing κ_L. Consequently, κ_L was reduced to 0.30 $W{\cdot}m^{-1}{\cdot}K^{-1}$, yielding a peak $ZT \approx 0.9$ at 676 K and an average $ZT \approx 0.52$ across 323–676 K.[77]

A twin boundary is a planar defect across which the crystal lattice is mirrored. Twins typically form during processes such as plastic deformation, annealing, or rapid solidification, where stress or thermal driving forces promote coordinated lattice reorientation. Coherent nanotwins, which retain an ordered atomic registry across the boundary, preferentially scatter mid- to low-frequency phonons while leaving carrier mobility largely intact; this selectivity can enhance thermoelectric performance by reducing lattice thermal conductivity without severely degrading electrical transport. Li *et al.*[25] introduced dense twin networks into Cu_2SnS_3 by mechanical alloying followed by spark-plasma sintering; the twin engineering reduced the lattice thermal conductivity to ~ 0.46 $W{\cdot}m^{-1}{\cdot}K^{-1}$ at 773 K and yielded a peak $ZT \approx 0.98$. By contrast, CTS samples synthesized without twin engineering (e.g., by conventional solid-state or wet-chemical routes) display much higher κ_l (≈ 2.4 $W{\cdot}m^{-1}{\cdot}K^{-1}$ at ~ 320 K), underscoring the effectiveness of twin engineering in suppressing lattice heat transport.[78,79] Zheng *et al.*[80] fabricated core–shell Cu_5FeS_4 nano-icosahedra via a colloidal route, producing high densities of coherent twin planes. By reducing particle size (to ~ 130 nm) through Cu/Fe precursor tuning, they increased twin density ($\sim 1.6\times10^{-1}$ nm^{-1}) and obtained bulk samples with $\kappa_l \approx 0.45$ $W{\cdot}m^{-1}{\cdot}K^{-1}$ at 773 K and a peak $ZT \approx 0.95$, illustrating the effectiveness of "twin + composition" engineering for simultaneous phonon suppression and electrical optimization. High twin-plane densities can decouple phonon and carrier transport by matching the twin spacing to dominant phonon mean free paths while remaining much larger than electronic mean free paths, thus preferentially scattering phonons over charge carriers.

Stacking faults, which arise from deviations in the atomic stacking sequence, scatter phonons and thereby reduce the lattice thermal conductivity κ_L, improving thermoelectric performance. Such faults emerge during plastic deformation, rapid annealing, or alloying, for example when an FCC sequence shifts from ABCABC$\cdots$ to ABCACB$\cdots$. In Cd-doped high-entropy $PbSe_{0.5}S_{0.25}Te_{0.25}$, lattice mismatch at the rock-salt PbSe/CdS interfaces generates interfacial strain that is relaxed via the formation of dense stacking faults.[26] These stacking faults act as efficient scattering centers for mid-frequency phonons, thereby reducing the κ_L. Analogous nanoscale stacking faults have been reported to scatter phonons in $TlGaSe_2$[81] and in $(GeTe)_{1-x}(Bi_2Te_3)_x$[82] composites, contributing to suppressed κ_L in those systems. Ming *et al.*[83] deliberately engineered dense stacking-fault networks in Cu_2SnSe_3 by lowering the intrinsic stacking-fault energy; the resulting planar defects strongly impede heat-carrying phonons and reduce κ_L.

Overall, in bulk nanostructured materials, the primary strategy for reducing thermal conductivity is to modify the lattice structure. Introducing defects increases phonon scattering centers and shortens phonon relaxation times. Among various types of defects, linear and planar defects enhance phonon scattering without significantly degrading carrier mobility, unlike point defects. Furthermore, planar defects can selectively scatter low-energy carriers and mid-frequency phonons, making them a highly promising approach for concurrently lowering thermal conductivity and enhancing the Seebeck coefficient.

2.2. Phonon group velocity and specific heat modulation

2.2.1. Phonon group velocity

Lattice thermal conductivity depends critically on the phonon group velocity v_g, which, for long-wavelength acoustic modes, is commonly approximated by the sound velocity v_s. Low sound velocities generally correlate with low lattice thermal conductivities. Phonon dynamics are governed by the nature and strength of chemical bonding: the sound velocity scales as $v_s \sim \sqrt{k/M}$, where k denotes the bond stiffness (force constant) and M the average atomic mass.[84] Consequently, weak bonds and heavy constituent elements yield low v_s and hence reduced lattice thermal conductivity.[84]

Liu *et al.*[27] investigated Cd substitution in p-type zintl AB_2X_2 compounds (A = Mg, Ca, Ba, Sr, Yb, Eu; B = Zn, Cd, Mg; X = Sb, Bi) using density-functional theory, combin-

ing chemical-bond analysis with electron-localization (ELF) mapping. Figure 7(a) presents the ELF on the (100) plane of $Ca_8Mg_{14}Cd_2Bi_{16}$; by definition, ELF = 1 corresponds to perfect localization, ELF = 0.5 to a homogeneous electron gas and ELF = 0 to complete delocalization. The ELF around Ca sites remains essentially unchanged, indicating that Cd substitution at Mg sites does not alter the interlayer ionic character. Conversely, the reduced ELF between Cd and Bi (relative to Mg–Bi) indicates a weakening of covalent bonding within the *B*–*X* framework. Phonon-dispersion calculations (Figs. 7(b) and 7(c)) reveal pronounced softening of acoustic modes in $Ca_8Mg_{14}Cd_2Bi_{16}$: the cutoff frequencies at the *K* and *L* points decrease from 1.66 THz and 0.89 THz to 0.67 THz and 0.61 THz, respectively.[27] This lattice softening, together with enhanced phonon scattering, accounts for the observed reduction in κ_L. Similarly, Tian *et al.*[28] reported that substituting Ag for Mn in $MnSb_2Te_4$ weakens chemical bonding and induces lattice softening, producing an $\sim$ 12% reduction in sound velocity. Consequently, the room-temperature thermal conductivity decreased from 0.90 $W{\cdot}m^{-1}{\cdot}K^{-1}$ to 0.55 $W{\cdot}m^{-1}{\cdot}K^{-1}$ ($\sim$ 39% reduction). Zhu *et al.*[85] experimentally demonstrated that Pb incorporation into GeTe weakens chemical bonding and breaks lattice symmetry, inducing lattice softening. This conclusion is supported by the flattening of low-frequency acoustic phonon branches and a concomitant decrease in phonon group velocity *v*, both of which lead to a pronounced reduction in lattice thermal conductivity.

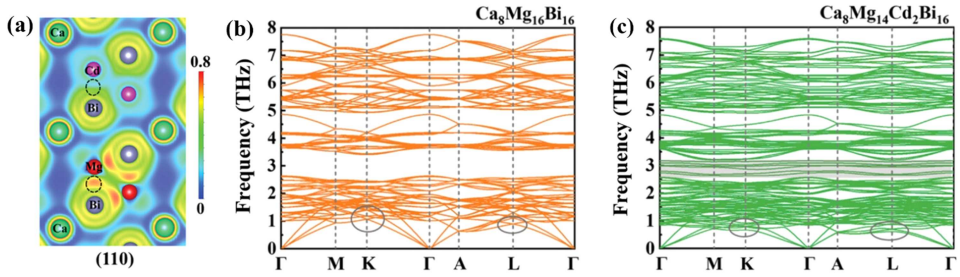


Fig. 7. (a) Calculated electron localization function (ELF) of (110) plane for supercell $Ca_8Mg_{14}Cd_2Bi_{16}$. Reproduced with permission from Ref. [27]. The Cd doping weakens the covalent bonding of the *B*–*X* framework as indicated by the smaller ELF value between Cd and Bi. The phonon dispersion of (b) $Ca_8Mg_{16}Bi_{16}$, and (c) $Ca_8Mg_{14}Cd_2Bi_{16}$. Reproduced with permission from Ref. [27].

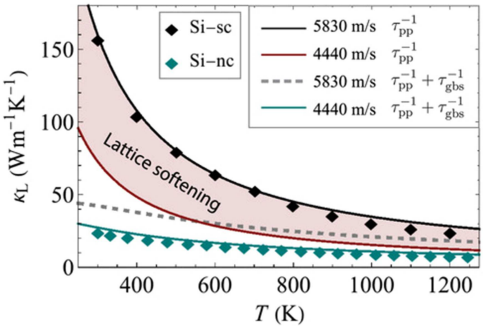


Fig. 8. Callaway-type model analysis of κ_L showing the separate contributions of lattice softening and phonon–grain-boundary scattering in the reduction of κ_L from single-crystal to nanocrystalline Si (average grain size $\approx$ 42 nm). Reproduced with permission from Ref. [29].

Unlike conventional defect-induced phonon scattering, lattice softening remains effective across a broad temperature range and consistently reduces the κ_L. Hanus *et al.*[29] systematically demonstrated this distinction. In their schematic comparison (Fig. 8),[29] solid circles denote experimental κ_L for single-crystal Si (sc-Si) and nanocrystalline Si (nc-Si; average grain size $\approx$ 42 nm), while the curves show calculated κ_L that include lattice-softening effects and/or scattering mechanisms (phonon–phonon scattering τ_{pp}^{-1} and phonon–grain-boundary scattering τ_{gbs}^{-1}). The only parameters changed between sc-Si and nc-Si were the sound velocity v_s and the grain size, both measured experimentally. The reduction from the black to the yellow curve reflects lattice softening alone, whereas the drop to the blue dashed curve reflects grain–boundary scattering; when both mechanisms are included (blue solid curve), the calculated κ_L closely matches the nc-Si data over the entire temperature range. Notably, phonon scattering dominates at low temperatures but becomes progressively less effective at high temperatures, whereas lattice softening yields a nearly uniform reduction in κ_L across all temperatures, as shown in Fig. 8.[29]

Doping or alloying is a widely used strategy to induce lattice softening. Han *et al.*[86] reported that substituting Hf or Ta for Nb in NbFeSb, owing to the large atomic masses and, in the case of Hf, its aliovalent character, produces avoided crossings between optical and acoustic phonon branches and reduces the acoustic phonon group velocity. With 10% Ta or Hf substitution, the phonon group velocity V_g decreases from 3428 $m{\cdot}s^{-1}$ to 3388 $m{\cdot}s^{-1}$ (Ta) and 3349 $m{\cdot}s^{-1}$ (Hf); 10% Hf doping in particular yields a $\sim$ 65% reduction in lattice thermal conductivity. Xiang *et al.*[87] synthesized $Zr_3Ni_{2.5}Co_{0.5}Sb_4$ by Co-doping $Zr_3Ni_3Sb_4$; phonon dispersions reveal strong flattening of optical branches and a reduction of the acoustic cutoff frequency from 95 cm^{-1} to $\leq$ 65 cm^{-1}, consistent with pronounced lattice softening. Ni–Co disorder further introduces localized rattler-like modes that undergo avoided crossings with low-frequency acoustic phonons, flattening the branches and extending phonon lifetimes in that frequency window; consequently, the lattice thermal conductivity is reduced by $\sim$ 42%.

A heavy alloying approach, such as incorporating $AgSbTe_2$ into $MnGeTe_2$, can simultaneously modulate both electronic and lattice properties. The heavier Ag and Sb atoms enhance spin–orbit coupling and increase the density-of-states effective mass (m^*) by approximately 50%, while maintaining a high Seebeck coefficient at elevated hole concentrations.[88] Alloying also softens the lattice: both transverse and longitudinal sound velocities decrease with increasing $AgSbTe_2$ content, which suppresses κ_L toward the amorphous limit. Shen *et al.*[89] showed that substituting Cd for Zn in ZnSb produces strong point-defect scattering and concurrently softens acoustic phonons, leading to an approximately 44% reduction in κ_L at room temperature for $Zn_{0.7}Cd_{0.3}Sb$.

Moreover, internal strain fields introduced by structural defects can induce lattice softening. For example, Shen *et al.*[90] reported that excess Ag in $AgIn_5Se_8$ generates abundant point defects, twin boundaries and stacking faults; these defects produce internal strain fields that soften the lattice and enhance phonon scattering, thereby reducing the κ_L. As the Ag content x increases from 0 to 0.03 and 0.07, the average sound velocity v_s decreases from 2028 $m{\cdot}s^{-1}$ to 1905 $m{\cdot}s^{-1}$ and 1674 $m{\cdot}s^{-1}$, respectively. Similarly, materials containing high dislocation densities (for example, $Na_{0.03}Eu_{0.03}Sn_{0.02}Pb_{0.92}Te$)[91] exhibit strain-induced phonon softening and corresponding κ_L suppression. Distinct from direct phonon–dislocation scattering, the strain fields associated with dense dislocation networks reduce the local sound velocity through localized anharmonicity, which in turn suppresses κ_L (κ_L scales approximately with v_s^3),[92] thus providing an efficient route to lower thermal conductivity without necessarily introducing strong carrier scattering.

2.2.2. Specific heat

Reducing specific heat alone offers limited leverage for lowering thermal conductivity because, under the Debye approximation, the high-temperature heat capacity of a crystalline solid approaches the Dulong–Petit limit ($c_v \approx 3Nk_B$). Superionic conductors circumvent this constraint: above the superionic transition temperature, mobile cations become highly disordered and exhibit liquid-like dynamics. Local hopping and atomic rearrangements in the cation sublattice suppress shear-wave propagation and disrupt phonon heat transport, so that c_v can decrease from $\sim 3Nk_B$ to roughly 2–$2.5Nk_B$ and the lattice thermal conductivity is substantially reduced. For example, $Cu_{2-x}Se$ — where a rigid Se sublattice coexists with a liquid-like Cu sublattice — has been reported to attain $ZT \approx 1.5$ near 1000 K, an effect attributed to the suppression of transverse phonon modes by the mobile Cu ions.[93] Likewise, in $Ag(Cu)CrSe_2$, the onset of superionic disorder of Ag/Cu on tetrahedral sites leads to pronounced anharmonicity and strong phonon scattering, which reduces c_v and yields ultralow lattice thermal conductivity.[30] These examples illustrate that superionicity provides an alternative route to lower κ_L via changes in both specific heat and phonon transport, complementary to strategies based on increased phonon scattering alone.

Table 1. Comparison of phonon-engineering strategies.

Strategy	Main affected phonon band	Typical advantages	Typical disadvantages	Practical applicability scalability
Point defects	High frequency; Rayleigh scattering $\propto \omega^4$	Strong suppression of high-frequency phonons; doping can tune carrier concentration	Often scatters charge carriers and reduces mobility; requires tight control of defect level to balance S and σ	Simple, low-cost processing (doping); widely used, but electronic penalties must be managed
Linear defects	Mid-frequencies ($\tau \sim \omega^{-1}$–ω^{-3} components)	Efficient mid-frequency scattering; can lower κ_L with limited mobility loss if engineered; stress fields assist scattering	Requires very high dislocation density for large effect; difficult to produce while preserving electronics	Multiple lab-scale methods exist (UHP, LPS, hot deformation); industrialization must balance performance and cost
Interfaces	Low to mid-low frequencies (long-wavelength modes); interface scattering $\sim \omega^0$	Very effective for low-frequency phonons; coherent twins can preserve carrier mobility	Excessive or very fine interfaces may also scatter carriers; trade-off between thermal and electrical transport	Scalable via powder metallurgy, thermomechanical processing and precipitation engineering; requires control of interface stability
Lattice softening	Broadband (reduces sound speed v_g; affects whole spectrum)	Effective across temperatures; continuously lowers κ_L and is stable at high T	Often relies on heavy/toxic elements (e.g., Pb, Te); can alter electronic DOS (positive or negative)	Readily scalable by alloying, but toxicity and resource cost must be managed; band-structure impacts need optimization
Superionic behavior	Suppresses transverse modes; reduces effective c_v in superionic temperature window	Can strongly lower κ_L at high T via distinct mechanisms (changes c_v and modal behavior)	Requires high T; possible phase/chemical instability; limited operating window	Suitable for high-T applications ($\sim$ 800–1000 K); long-term stability limits industrial use

Modifying the lattice architecture of bulk nanostructured materials is a principal strategy to suppress κ_L. Defect engineering introduces scattering centers that shorten phonon relaxation times: point defects predominantly scatter high-frequency phonons, dislocations target mid-frequency modes, and interfaces or planar faults (e.g., nanotwins, low-angle grain boundaries) impede low-frequency, long-wavelength phonons. Unlike point defects, which often degrade carrier

mobility, well-designed one- and two-dimensional defects can scatter phonons effectively while preserving or even improving electronic transport via energy-filtering effects, thereby providing simultaneous reduction of κ_L and enhancement of the Seebeck coefficient. Complementary approaches include lattice softening — via mass substitution or alloying — that reduces phonon group velocities (v_g), and superionic behavior, in which liquid-like cation dynamics suppress transverse phonons and lower the effective specific heat (c_v); both mechanisms reduce κ_L across broad temperature ranges. As shown in Table 1, a comparison of phonon-engineering strategies is summarized, including the primary phonon frequency ranges they target, their typical advantages and disadvantages, and the practical limitations of their applications. Crucially, these mechanisms act synergistically: by combining phonon scatterers that operate at different frequency bands with lattice-softening or superionic effects, one can suppress thermal transport across the whole phonon spectrum while retaining favorable electronic properties. This multi-scale, multi-mechanism paradigm therefore offers a robust route to approaching the phonon-glass, electron-crystal ideal and to realizing high-performance thermoelectric materials.

3. Phonon engineering of low-dimensional structures

Despite their success in three-dimensional systems, conventional phonon-engineering strategies still face a fundamental limitation: the trade-off between the Seebeck coefficient and electrical conductivity as carrier concentration varies, which constrains further ZT improvements. In 1993, Hicks and Dresselhaus[32] proposed that low dimensionality and quantum-confinement effects can sharpen the electronic density of states near the Fermi level and thereby increase the Seebeck coefficient, while surface and interface scatterings preferentially suppress phonon transport.[33–35] Building on this idea, micro- and nanostructuring, including superlattices, nanocomposites, and nanowires, has been developed to decouple electronic and phononic transport and to achieve substantially reduced lattice thermal conductivity and enhanced thermoelectric performance.

3.1. Superlattices

Superlattice thin films are periodic structures formed by stacking alternating layers of two or more materials, with individual layer thicknesses typically ranging from a few to several tens of atomic layers. Phonon transport in such superlattices can be either incoherent (particle-like) or coherent (wave-like), depending on the relation between the phonon mean free path (or coherence length) and the superlattice period. When the phonon mean free path is shorter than the period, transport is dominated by incoherent particle-like phonons and can be described by particle-based models in which phonons scatter independently at interfaces; conversely, when the period is comparable to or smaller than relevant phonon wavelengths or coherence lengths, wave effects and coherent transport become significant. In the incoherent regime, thermal conductivity is effectively reduced by enhancing interface scattering — for example, by increasing interface density or roughness, introducing nano-inclusions, or maximizing the mismatch in phonon density of states between constituent layers. Superlattice films are commonly fabricated by sputtering,[94] thermal evaporation,[95] metal–organic chemical vapor deposition (MOCVD)[96] and molecular beam epitaxy (MBE),[34] each providing different trade-offs between interface sharpness, compositional control and throughput.

Recent advances in epitaxial-film synthesis enable atomic-scale engineering of phononic states. Superlattices (SLs), i.e., periodic stacks of alternating layers, redefine lattice periodicity via a supercell of thickness Na (where N is the number of unit cells and a is the unit-cell thickness). This produces zone folding of the phonon dispersion and reduces the Brillouin zone to $2\pi/Na$.[99] At the reduced zone, zone-folded acoustic (ZA) phonons appear (Fig. 9(a)) and their energies are tunable through N.[97] When Na is shorter than the phonon coherence length λ (coherent regime, $\lambda > Na$), wave interference opens gaps at the zone boundary; ZA modes form standing waves at these gaps and the thermal conductivity κ is reduced. Hence κ tends to decrease as Na increases (stronger zone folding). Conversely, when Na is much larger than λ (incoherent regime, $\lambda < Na$), scattering destroys coherence, the zone-folding gaps close, and k increases with Na despite the larger number of zone folds.[97] As a result κ is non-monotonic and reaches a minimum near the coherence–incoherence crossover ($Na \approx \lambda$). Because phonon coherence depends on the relative lengths Na and λ, κ can be engineered either geometrically (by changing Na) or by tuning λ through phonon renormalization associated with electronic or magnetic phase transitions.[100] Recent studies of oxide SLs stress that designing both the electronic contribution to thermal conductivity and the phonon spectrum is essential to realize high thermoelectric performance.[100] Although artificial, zone-folded phonons in SLs are now well established, modulation of these modes by correlated electronic or magnetic phase transitions remains uncommon. Recent experiments on oxide superlattices illustrate how control of phonon coherence and zone folding tunes thermal transport. For example, $SrRuO_3/SrTiO_3$ superlattices show a clear coherence–incoherence crossover: by varying the interface density $n = 2/Na$ (with Na the supercell thickness), the cross-plane thermal conductivity κ displays a minimum at $n \approx 0.7$ nm^{-1} ($Na \approx 2.8$ nm), corresponding to $\lambda \approx 2.8$ nm The minimum κ is ~ 2.1 W·m^{-1}·K^{-1}, slightly above the alloy limit, and the measured n dependence is quantitatively cap-

tured by Simkin–Mahan calculations that include zone-folding effects.[97] TDTR, Raman and SHG measurements show that structural phase transitions (polar/AFD ordering and ferromagnetism) in the constituent layers strongly modify phonon coherence and mean free paths; temperature- or strain-driven symmetry changes therefore can further suppress κ by disrupting coherence and opening or closing zone-folding gaps. These results demonstrate that superlattice geometry combined with correlated structural and electronic phase transitions provides powerful, complementary levers to suppress heat transport by phonon engineering.[97] Fu *et al.*[101] fabricated Bi_2Te_3/Sb_2Te_3 superlattices and reported a reduced thermal conductivity of 0.33 $W{\cdot}m^{-1}{\cdot}K^{-1}$ at 275 K, compared with 2.38 and 1.56 for bulk Sb_2Te_3 and Bi_2Te_3, respectively; the reduction was attributed to enhanced phonon scattering from the SL's high interface density. Similarly, Yang *et al.*[98] prepared Sb_2Te_3–Sb_2Se_3 superlattice films whose room-temperature κ is lower than that of single-component Sb_2Te_3; in particular, a sample with 2 nm:2 nm layer thicknesses exhibited $\kappa = 0.62$ $W{\cdot}m^{-1}{\cdot}K^{-1}$, nearly half that of Sb_2Te_3 (1.23 $W{\cdot}m^{-1}{\cdot}K^{-1}$), demonstrating the effectiveness of SL architectures in suppressing heat transport (Fig. 9(b)).

When the phonon mean free path (MFP) is comparable to or exceeds the superlattice period, phonons display wave-like behavior: they can coherently propagate across several periods, preserve phase information and undergo multiple reflections at interfaces. Under these conditions, coherent transmission and multiple-interface reflections produce interference effects that modify phonon dispersion, opening or widening phononic band gaps and reducing phonon group velocities. Introducing aperiodicity can disrupt coherent transport and promote phonon localization, thereby yielding ultralow thermal conductance in suitably designed superlattices.[102–104] For example, Hu *et al.*[105] reported that aperiodic Si/Ge superlattices can exhibit thermal conductivities an order of magnitude lower than periodic counterparts, which they attributed to Anderson localization of coherent phonons. Jue Wang and co-workers[106] theoretically examined periodic and two classes of aperiodic MoS_2–$MoSe_2$ lateral superlattices, finding that increasing the length of the aperiodic region reduces phonon conductance and can induce localization; the most strongly aperiodic ('wild') structures show the lowest conductance for a given length. Phonon transmission analysis indicates that suppressed transmission in these lateral superlattices stems from enhanced anharmonic scattering and interface disorder, which together reduce κ_L and improve the thermoelectric figure of merit. Finally, tuning the interlayer twist angle in van der Waals heterostructures provides an additional route to modulate phonon transport: studies report a strong, material-dependent twist-angle dependence of thermal conductivity, although the absolute magnitudes vary with the system and measurement or computational details. Moreover, tuning the interlayer twist angle of the superlattice provides another pathway to further reduce the lattice thermal conductivity. For example, Singh *et al.*[107] twisted the interlayer angle of CrI_3/1T-MoS_2, achieving ultralow lattice thermal conductivities of 0.0341 $W{\cdot}m^{-1}{\cdot}K^{-1}$ and 0.0034 $W{\cdot}m^{-1}{\cdot}K^{-1}$ at twist angles of 23.41° and 30°, respectively.

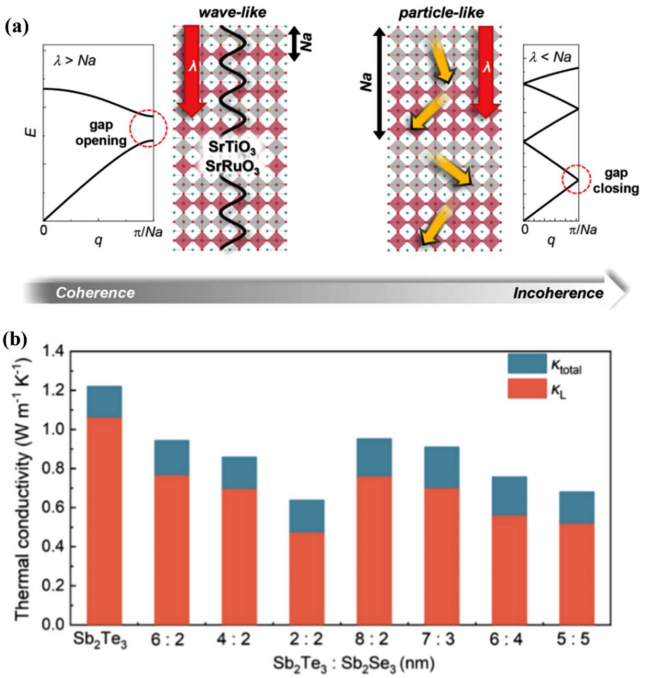


Fig. 9. (a) Coherent and incoherent phonon transport in $SrRuO_3/SrTiO_3$ superlattice (SRO/STO SL). Reproduced with permission from Ref. [97]. (b) Total thermal conductivity and lattice thermal conductivity of Sb_2Te_3–Sb_2Se_3 thin films and the comparison with reported data at room temperature. Reproduced with permission from Ref. [98].

3.2. Nanowires

Nanowires, as prototypical one-dimensional materials, have diameters that are much smaller than those of bulk counterparts, which enhances phonon boundary scattering. Silicon nanowires (Si-NWs) are particularly promising for thermoelectric applications because they can substantially reduce thermal conductivity while largely preserving the Seebeck coefficient and electrical conductivity of bulk silicon. Lee *et al.*[108] systematically tuned the Si-NW diameter, doping level and surface roughness to optimize phonon scattering. They found that reducing the nanowire cross-sectional area intensifies phonon–boundary scattering and markedly lowers thermal conductivity, and increasing surface roughness introduces additional scattering sites that further suppress the heat transport.

Figures 10(a) and 10(b) compare measured thermal conductivities for vertical Si-NWs as a function of diameter and roughness; Fig. 10(a) additionally includes data for vapor–liquid–solid (VLS)-grown Si-NWs. For example, increasing the root-mean-square surface roughness from 2.28 nm to 6.88 nm reduces thermal conductivity by $\sim 25.5\%$, and decreasing the diameter from 350 nm to 200 nm yields an additional $\sim 27.5\%$ reduction. Phonon mean-free-path calcu-

lations indicate that rough surfaces predominantly suppress long-wavelength phonons, whereas diameter reduction shortens the MFP across a broad portion of the phonon spectrum. Furthermore, B- and P-doped Si-NWs (200-nm diameter) exhibit thermal conductivities 71.5% and 58.4% lower than those of undoped rough wires, corresponding to values $\sim 14.8\times$ and $\sim 10.1\times$ smaller than bulk silicon (150 $W{\cdot}m^{-1}{\cdot}K^{-1}$), respectively. Kang *et al.*[109] synthesized tellurium nanowires with a thermal conductivity of ~ 1.0 $W{\cdot}m^{-1}{\cdot}K^{-1}$ — substantially lower than bulk Te pellets — and Shah *et al.*[110] showed that surface passivation of Te nanowires can further reduce thermal conductivity to ~ 0.16 $W{\cdot}m^{-1}{\cdot}K^{-1}$ by enhancing phonon scattering at nanowire–matrix interfaces. Heris *et al.*[111] examined how transverse cross-sectional geometry affects the thermal conductivity of Si and Ge nanowires by comparing circular, triangular, diamond, hexagonal, and square profiles. They found that nanowires with more edges or corners exhibit lower thermal conductivity and that conductivity increases with the cross section's surface-to-volume ratio (perimeter-to-area ratio). Extending their work, they modeled hollow nanowires by removing core atoms and observed significant conductivity reductions across all geometries. This decline stems from the hollow design's further increase in surface-to-volume ratio, which enhances phonon confinement and scattering, yielding much lower thermal conductivity than in solid nanowires.

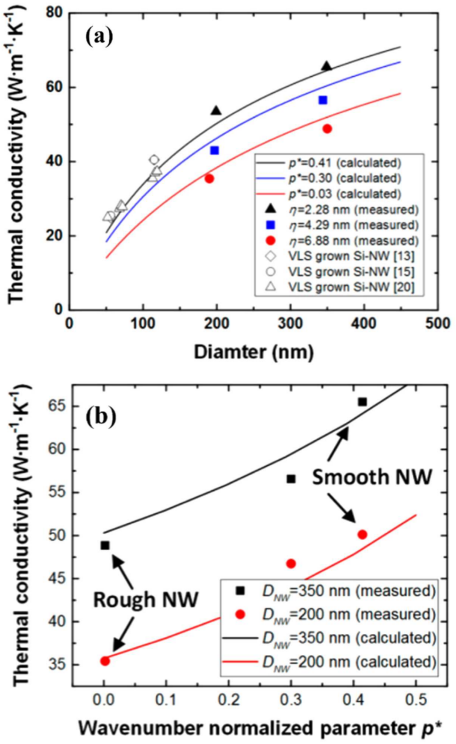


Fig. 10. (a) Thermal conductivity of various vertical Si-NWs (filled symbol: measured data, empty symbol: previously reported data in the literatures, solid line: calculated value using p^*). Reproduced with permission from Ref. [108]. (b) Thermal conductivity of vertical Si-NWs with DNW of 200 nm (red) and 350 nm (black) as a function of normalized specular parameter p^* related with η (filled symbol: measured data, solid line: calculated value using p^*). Reproduced with permission from Ref. [108].

3.3. Nanocomposites

Nanocomposites are nano-heterostructures in which nanoscale inclusions, such as fine grains or nanoparticles, are embedded within a host matrix and act as additional phonon-scattering centers.[112] In this review, the term "nanocomposites" specifically refers to bulk matrices containing nanoscale inclusions whose thermal transport is governed by interfacial scattering and related nanoscale effects. When the inclusions are metallic or semimetallic, they can donate electrons to increase electrical conductivity and generate an energy-filtering effect that enhances the Seebeck coefficient. For example, Zheng *et al.*[113] fabricated a hybrid 0D–2D heterostructure by *in situ* growth of Au nanoparticles on hexagonal Sb_2Te_3 nanoplates; this architecture simultaneously optimized electrical conductivity, thermal conductivity and the Seebeck coefficient, yielding an $\sim 110\%$ increase in ZT relative to pristine Sb_2Te_3. Kim *et al.*[114] reported that incorporation of an Sb_2O_3 nanophase into $Bi_{0.5}Sb_{1.5}Te_3$ enhanced the Seebeck coefficient via energy filtering and reduced thermal conductivity by $\sim 77\%$ owing to strong phonon scattering at interfaces. Building on this concept, Minsu Kim and co-workers[115]constructed 1D/2D nanocomposites comprising Sb_2O_3 nanowires and layered double hydroxides (LDHs); the resulting increase in 1D/2D heterointerface density produced intense interfacial phonon scattering, effectively suppressing lattice thermal conductivity and improving ZT.

Low-dimensional architectures such as superlattices, nanowires and nanocomposites provide tunable parameters at the length and interface scales that facilitate partial decoupling of electronic and phononic transport, thereby substantially suppressing κ_L and improving thermoelectric performance. Superlattices operate in two transport regimes: an incoherent regime dominated by interface scattering and a coherent regime dominated by wave interference. In the incoherent regime, increasing interface density, enhancing interface roughness or introducing aperiodicity strengthens interface scattering. In the coherent or semi coherent regime, multiple-interface reflections and interference can open phononic band gaps or induce phonon localization, which reduce phonon group velocities and κ_L. Nanowires intensify boundary and geometric scattering through diameter reduction, increased surface roughness, modified cross sectional shapes or hollow architectures; doping and surface treatments can act synergistically to lower κ_L while preserving or improving electronic transport. Nanocomposites introduce additional interfacial scattering centers by embedding nanoscale inclusions within a host matrix. When inclusions are metallic or semimetallic, they can also provide charge donation or energy filtering to optimize electronic properties. Experimental demonstrations confirm the efficacy of low-dimensional designs for dramatically reducing κ_L and enhancing ZT. Overall, by tuning interface density, size, surface roughness, aperiodicity and in-

terlayer twist, low-dimensional phonon engineering supplies a multiscale, multimodal toolbox to minimize heat conduction without sacrificing electronic performance; however, controllable fabrication, interface precision and scalable manufacturability remain major challenges for practical deployment

4. Conclusion

The pursuit of high thermoelectric performance has motivated extensive efforts towards designing materials with intrinsically low lattice thermal conductivity. This review examines the role of phonon engineering in reducing lattice thermal conductivity and summarizes recent advances in two complementary approaches, namely, phonon engineering of bulk nanostructured systems and phonon engineering of low-dimensional materials.

In bulk nanostructured systems, defect engineering introduces scattering centers that selectively target phonons across the frequency spectrum. Point defects effectively scatter high frequency phonons and can concurrently tune carrier concentration. Dense dislocation networks mainly suppress mid-frequency phonons and may be generated by doping, vacancy clustering, liquid phase extrusion, hot deformation or ultrahigh pressure sintering. Interfacial defects such as grain boundaries, twin planes and stacking faults preferentially impede low frequency long wavelength phonons while exerting limited influence on carrier mobility. Lattice softening and modulation of specific heat provide additional suppression of lattice thermal conductivity: heavy atom substitution, alloying and bond weakening reduce phonon group velocities, whereas superionic behavior characterized by liquid like cation dynamics lowers the effective heat capacity and suppresses transverse phonon transport. Importantly, these mechanisms can act synergistically so that combining frequency targeted scattering with lattice softening or superionic effects suppresses heat conduction across the full phonon spectrum while preserving favorable electronic properties.

Phonon engineering in low dimensional materials offers further opportunities to reduce lattice thermal conductivity. Architectures such as superlattices, nanowires and nanocomposites provide tunable design levers through length scale and interface engineering, enabling more effective decoupling of electronic and phononic transport. Superlattices may operate in an incoherent regime dominated by interface scattering or in a coherent regime dominated by wave interference; increasing interface density, enhancing interface roughness or introducing aperiodicity strengthens phonon scattering, while in the coherent regime multiple reflections and interference can open phononic band gaps or induce localization, both of which reduce phonon group velocities and thermal conductivity. Nanowires enhance boundary and geometric scattering through diameter reduction, increased surface roughness, cross sectional design or hollow architectures; appropriate doping and surface treatments can further suppress lattice thermal conductivity while maintaining or improving electrical transport. Nanocomposites formed by embedding metallic, semimetallic or insulating nanoprecipitates in a host matrix generate abundant interfacial scattering sites and, when metallic inclusions are used, can enable energy filtering or charge transfer to optimize electronic properties. Numerous experimental demonstrations confirm that low dimensional designs can substantially reduce lattice thermal conductivity and enhance the thermoelectric figure of merit.

The practical relevance of these strategies, however, hinges on manufacturability, cost and environmental considerations — topics discussed next. From a translational perspective, practical deployment requires careful assessment of process, economic and environmental factors. Many phonon engineering approaches, notably point defect doping and nanocomposite formation, are compatible with conventional metallurgical and powder metallurgy routes such as alloy melting and ball milling followed by hot pressing, and thus have scale up potential. Powder metallurgy methods including gas atomization and low temperature pulverization, together with emerging ink based printing techniques, show promise for higher throughput and lower cost device fabrication.[116–118] By contrast, laboratory scale, atomically precise strategies such as molecular beam epitaxy grown superlattices and twist engineering of van der Waals heterostructures remain slow and costly and therefore face substantial barriers to industrialization.[119] Material supply and environmental constraints further complicate route selection, because many high performance systems rely on scarce or toxic elements, notably Te and Pb, which pose supply risk and health concerns and motivate research on Pb and Te free alternatives.[120,121] Finally, a persistent trade off exists between κ_L suppression and electronic transport: many effective phonon scattering motifs reduce κ_L but simultaneously increase carrier scattering, degrading mobility and electrical conductivity. Strategies such as energy filtering, band engineering to increase density of states effective mass, and careful matching of phonon and electron scattering length scales can mitigate these penalties, but they add design complexity and require extensive optimization.

In summary, integrating multiscale, multimodal phonon control strategies can substantially reduce lattice thermal conductivity while preserving electronic performance, thereby advancing the phonon glass electron crystal paradigm. To translate high performance concepts into manufacturable devices, future research should prioritize scalable processing routes and environmentally benign chemistries.

Acknowledgements

This work was supported by the National Key R&D Program of China (Grant No. 2022YFB4602401), the National

Natural Science Foundation of China (Grant No. 51706039), the Fundamental Research Funds for the Central Universities (Grant No. 2572020BF01), the CAS-XDC Project (Grant No. XDC0150303), and the Innovation Foundation for Doctoral Program of Forestry Engineering of Northeast Forestry University (Grant No. LYGC202216).

References

[1] Wu C, Shi X L, Wang L, Lyu W, Yuan P, Cheng L, Chen Z G and Yao X 2024 *ACS Nano* **18** 31660
[2] Miao Z, Meng X and Liu L 2022 *J. Power Sources* **541** 231699
[3] Zeng L, Deng D, Zhu L, Zhang Z, Gu X, Wang H and Jiang Y 2024 *Nano Energy* **125** 109531
[4] Fan W, An Z, Liu F, Gao Z, Zhang M, Fu C, Zhu T, Liu Q and Zhao X 2023 *Adv. Sci.* **10** 2206397
[5] Li X, Xie C, Quan S, Shi Y and Tang Z 2019 *IEEE Access* **7** 72143
[6] Alam N, Ali M S, Sajid S, Sharma D and Hasan Z 2023 *Solar Energy* **263** 111892
[7] Liu X, Zheng F, Fu Q, Song G and Xiong Y 2024 *Appl. Therm. Eng.* **244** 122763
[8] Assylbekova L, Aldiyarov N, Yevdulov O and Kuldeev N 2024 *Bio-NanoScience* **14** 1428
[9] Shi X L, Zou J and Chen Z G 2020 *Chem. Rev.* **120** 7399
[10] Yang H, Jia B, Xie L, Mao D, Xia J, Yang J, Yuan M, Gan Q, Liu X and Hu M 2024 *Joule* **8** 2667
[11] Lin S, Wang S, Li Y, Lai Z, Yang X, Lu X and Jin M 2024 *Acta Metall. Sin. (Engl. Lett.)* 1–10
[12] Yin Y, Baskaran K and Tiwari A 2019 *Physica Status Solidi (a)* **216** 1800904
[13] Ye H and Zhou C 2025 *Acta Metall. Sin. (Engl. Lett.)* **38** 720
[14] Xie S, Zhu H, Zhang X and Wang H 2023 *IJEM* **6** 012007
[15] Chang Z, Liu K, Sun Z, Yuan K, Cheng S, Gao Y, Zhang X, Shen C, Zhang H and Wang N 2022 *IJEM* **4** 025001
[16] Hu J, Zuo Y, Hao Y, Shu G, Wang Y, Feng M, Li X, Wang X, Sun J and Ding X 2023 *Chin. Phys. B* **32** 046301
[17] Ming H, Zhu C, Chen T, Yang S, Chen Y, Xin H, Zhang J, Li D and Qin X 2023 *Inorg. Chem.* **62** 2607
[18] Wang W Y, Zhu J L, Bo L, Zhou W Y, Liu X S, Li C C, Zhang Z and Zhao D G 2025 *Rare Met.* **44** 3339
[19] Karthikeyan V, Oo S L, Surjadi J U, Li X, Theja V C, Kannan V, Lau S C, Lu Y, Lam K H and Roy V A 2021 *ACS Appl. Mater. Interfaces* **13** 58701
[20] Ge B, Yu Y and Zhou C 2025 *Adv. Eng. Mater.* **27** 2500553
[21] Zhang D, He P, Liu G, Zhong R, Xu F, Yang J, Luo Y and Wang S 2024 *Scr. Mater.* **244** 116003
[22] Huang Z, Hayashi K, Saito W, Li H, Pei J, Dong J, Chiba T, Nan X, Zhang B P and Li J F 2025 *Small Methods.* **9** 2500385
[23] Xie Y, Deng Q, Yang Y, Luo Y, Ou W, Zhao Z, Luo J, Wu H and Ang R 2025 *Small* **21** 2408852
[24] Fu C, Wu H, Liu Y, He J, Zhao X and Zhu T 2016 *Adv. Sci.* **3** 1600035
[25] Li W, Luo Y, Ma Z, Li C, Yang B, Wei Y, Li X, Jiang Q, Liu X and Yang J 2024 *Acta Mater.* **265** 119587
[26] Jiang B, Yu Y, Chen H, Cui J, Liu X, Xie L and He J 2021 *Nat. Commun.* **12** 3234
[27] Liu M, Guo M, Zhu J, Zeng X, Chen H, Yuan D, Zhang Q, Cai F, Guo F and Zhu Y 2024 *Adv. Funct. Mater.* **34** 2316075
[28] Yu T, Zhang T, Qu X, Qi N, Yuan D, Su X, Tan G, Tang X and Chen Z 2025 *ACS Appl. Mater. Interfaces* **17** 14229
[29] Hanus R, Agne M T, Rettie A J, Chen Z, Tan G, Chung D Y, Kanatzidis M G, Pei Y, Voorhees P W and Snyder G J 2019 *Adv. Mater.* **31** 1900108
[30] Rana K S, Singh A, Bhui A, Biswas K and Soni A 2024 *ACS Appl. Energy Materials* **7** 5621
[31] Lin Y, Wood M, Imasato K, Kuo J J, Lam D, Mortazavi A N, Slade T J, Hodge S A, Xi K and Kanatzidis M G 2020 *Energy Environ. Sci.* **13** 4114
[32] Hicks L D and Dresselhaus M S 1993 *Phys. Rev. B* **47** 16631
[33] Yang X, Wang C, Lu R, Shen Y, Zhao H, Li J, Li R, Zhang L, Chen H and Zhang T 2022 *Nano Energy* **101** 107553
[34] Zhang C, Chen Z, Bai H, Lin W, Yang M, Hong M, Zhan F, Xie S, Zhang M and Li Z 2023 *Small* **19** 2300745
[35] Sang H, Wang W, Wang Z, Hong M, Zhang C, Xie S, Ge H, Yan F, Wang Z and Ouyang Y 2023 *Adv. Funct. Mater.* **33** 2210213
[36] Lyu W Y, Liu W D, Li M, Shi X L, Hong M, Cao T, Guo K, Luo J, Zou J and Chen Z G 2023 *J. Mater. Sci. Technol.* **151** 227
[37] Kim W, Zide J, Gossard A, Klenov D, Stemmer S, Shakouri A and Majumdar A 2006 *Phys. Rev. Lett.* **96** 045901
[38] Zhou C D, Liang B, Huang W J, Noudem J G, Tan X J and Jiang J 2023 *Rare Met.* **42** 2825
[39] Slack G A 1957 *Phys. Rev.* **105** 829
[40] Abeles B 1963 *Phys. Rev.* **131** 1906
[41] Wu M, Shi R, Qi R, Li Y, Feng T, Liu B, Yan J, Li X, Liu Z and Wang T 2023 *Chin. Phys. Lett.* **40** 036801
[42] Xie H, Su X, Hao S, Zhang C, Zhang Z, Liu W, Yan Y, Wolverton C, Tang X and Kanatzidis M G 2019 *J. Am. Chem. Soc.* **141** 18900
[43] Xiong Q, Han G, Wang G, Lu X and Zhou X 2024 *Adv. Funct. Mater.* **34** 2411304
[44] Wang S, Chang C, Bai S, Qin B, Zhu Y, Zhan S, Zheng J, Tang S and Zhao L D 2023 *Chem. Mater.* **35** 755
[45] Liu Y, Geng Y, Dou Y, Wu X, Hu L, Liu F, Ao W and Zhang C 2023 *Small* **19** 2303840
[46] Chen Z, Gao B, Tang J, Guo X, Li W and Ang R 2019 *Appl. Phys. Lett.* **115** 073903
[47] Tang Q, Jiang B, Wang K, Wang W, Jia B, Ding T, Huang Z, Lin Y and He J 2024 *Joule* **8** 1641
[48] Basu R and Singh A 2024 *Energy Adv.* **3** 689
[49] Ren K, Huo W, Chen S, Cheng Y, Wang B and Zhang G 2024 *Chin. Phys. B* **33** 057202
[50] Liu S, Wu D, Kong M, Wang W, Xie L and He J 2025 *ACS Energy Lett.* **10** 925
[51] Li J, Zhang X, Wang X, Bu Z, Zheng L, Zhou B, Xiong F, Chen Y and Pei Y 2018 *J. Am. Chem. Soc.* **140** 16190
[52] Li M, Shi X L and Chen Z G 2024 *Adv. Funct. Mater.* **34** 2403498
[53] Pei Y, Shi X, LaLonde A, Wang H, Chen L and Snyder G J 2011 *Nature* **473** 66
[54] Mandava S, Basu R, Khasimsaheb B, Bathula S, Singh A and Neeleshwar S 2021 *Mater. Adv.* **2** 4352
[55] Roychowdhury S and Biswas K 2018 *Chem* **4** 939
[56] Liu M, Zhu J, Cui B, Guo F, Liu Z, Zhu Y, Guo M, Sun Y, Zhang Q and Zhang Y 2022 *Cell Rep. Phys. Sci.* **3** 100902
[57] Wang W, Liu S, Wang Y, Jia B, Huang Y, Xie L, Jiang B and He J 2024 *Science Advances* **10** eadp4372
[58] Klemens P 1955 *Proc. Phys. Soc. A* **68** 1113
[59] Zheng Y, Slade T J, Hu L, Tan X Y, Luo Y, Luo Z Z, Xu J, Yan Q and Kanatzidis M G 2021 *Chem. Soc. Rev.* **50** 9022
[60] Wu R, Yu Y, Jia S, Zhou C, Cojocaru-Mirédin O and Wuttig M 2023 *Nat. Commun.* **14** 719
[61] Xu L, Xiao Y, Wang S, Cui B, Wu D, Ding X and Zhao L D 2022 *Nat. Commun.* **13** 6449
[62] Shi X, Chen H, Hao F, Liu R, Wang T, Qiu P, Burkhardt U, Grin Y and Chen L 2018 *Nat. Mater.* **17** 421
[63] Jung S H, Jo S, Song K, Choi E A, Bae J, Park J M, Hwang S M, Sun J Y, Kim H S and Kim K T 2024 *ACS Appl. Mater. Interfaces* **16** 39356
[64] Chen Q, Ji C, Yu J, Hua L and Zhao W 2025 *Ceram. Int.* **51** 26475
[65] Yin Z, Zhang H, Wang Y, Wu Y, Xing Y, Wang X, Fang X, Yu Y and Guo X 2025 *Adv. Energy Mater.* **15** 2403174
[66] Saito W, Hayashi K, Dong J, Li J F and Miyazaki Y 2020 *Sci. Rep.* **10** 2020
[67] Chen H, Savvides N, Dasgupta T, Stiewe C and Mueller E 2010 *Physica Status Solidi (a)* **207** 2523
[68] Liu S, Qin Y, Wen Y, Shi H, Qin B, Hong T, Gao X, Cao Q, Chang C and Zhao L D 2024 *Adv. Funct. Mater.* **34** 2315707
[69] Liu W D, Yin L C, Li L, Yang Q, Wang D Z, Li M, Shi X L, Liu Q, Bai Y and Gentle I 2023 *Energy Environ. Sci.* **16** 5123
[70] Chen B C, Wang K K and Wu H J 2022 *Mater. Today Phys.* **22** 100617
[71] Zhao D, Yang M, Sun H, Chen X, Zhang Y and Liu X 2023 *Chin. Phys. B* **32** 107305
[72] Zhou C, Lee Y K, Cha J, Yoo B, Cho S P, Hyeon T and Chung I 2018 *J. Am. Chem. Soc.* **140** 9282
[73] Huang K, Marthinsen K, Zhao Q and Logé R E 2018 *Prog. Mater. Sci.* **92** 284
[74] Mao H, Zeng C, Zhang Z, Shuai X and Tang S 2023 *Materials* **16** 6307

[75] Gomell L, Roscher M, Bishara H, Jaegle E A, Scheu C and Gault B 2021 *Scr. Mater.* **193** 153
[76] Li Y, Liu F, Ying B, Liu J, He Y, Liu K, Li A, Wu Y, Tang Z and Nan P 2024 *Mater. Today Phys.* **49** 101591
[77] Yang J, Ye H, Zhang X, Miao X, Yang X, Xie L, Shi Z, Chen S, Zhou C and Qiao G 2024 *Adv. Funct. Mater.* **34** 2306961
[78] Wei Y, Zhou Z, Jiang P, Zheng S, Xiong Q, Zhang B, Wang G, Lu X, Han G and Zhou X 2021 *ACS Appl. Energy Mater.* **4** 9240
[79] Zhou W, Dwivedi P, Shijimaya C, Ito M, Higashimine K, Nakada T, Takahashi M, Mott D, Miyata M and Ohta M 2018 *ACS Appl. Nano Mater.* **1** 4819
[80] Wei Y, Zhou Z, Wang H, Zheng S, Han G, Wang G, Zhang B, Lemoine P, Guilmeau E and Malaman B 2024 *Nano Energy* **131** 110181
[81] Simonian T, Roy A, Bajaj A, Dong R, Lei Z, Sofer Z, Sanvito S and Nicolosi V 2025 *npj 2D Mater. Appl.* **9** 46
[82] Kumar A, Rawat P, Kim J H, Thoravat S, Park J, Jin H and Rhyee J S 2024 *Mater. Chem. Phys.* **322** 129532
[83] Ming H, Zhu C, Chen T, Yang S, Chen Y, Zhang J, Li D, Xin H and Qin X 2022 *Nano Energy* **100** 107510
[84] Chen Z, Zhang X and Pei Y 2018 *Adv. Mater.* **30** 1705617
[85] Zhu J, Li R, Tan X, Feng F, Sun Q, Song P, Hong M and Ang R 2025 *Adv. Funct. Mater.* **35** 2417260
[86] Han S, Dai S, Ma J, Ren Q, Hu C, Gao Z, Duc Le M, Sheptyakov D, Miao P and Torii S 2023 *Nat. Phys.* **19** 1649
[87] Wei X, Guo Z, Li D, Li C, Sun B, Fu Y, Gao W and Liu Z 2024 *Mater. Today Phys.* **44** 101424
[88] Mei Q, Xie C, Liu J, Wang Y, Cui J, Liao L, Liao C, Xu W, Li S and Zhang Q 2025 *Adv. Eng. Mater.* **15** 2500937
[89] Shen D, Tai S T, Liu K, Wang W, Li H, Theja V C, Chen C and Chen Y 2025 *ACS Appl. Mater. Interfaces* **17** 17036
[90] Shen X, Zhang B, Chen Q, Tan H, Zhang X, Wang G, Lu X and Zhou X 2019 *Inorg. Chem. Front.* **6** 3545
[91] Wu Y, Chen Z, Nan P, Xiong F, Lin S, Zhang X, Chen Y, Chen L, Ge B and Pei Y 2019 *Joule* **3** 1276
[92] Yu Y, Cagnoni M, Cojocaru-Mirédin O and Wuttig M 2020 *Adv. Funct. Mater.* **30** 1904862
[93] Liu H, Shi X, Xu F, Zhang L, Zhang W, Chen L, Li Q, Uher C, Day T and Snyder G J 2012 *Nat. Mater.* **11** 422
[94] Hu B, Shi X L, Cao T, Li M, Chen W, Liu W D, Lyu W, Tesfamichael T and Chen Z G 2025 *Small Sci.* **5** 2300061
[95] Rasmi T, Bose R S C, Aarya P, Srikanth P, Haripriya V K and Malini K A 2025 *J. Alloys Compd.* **1034** 181378
[96] Han H, Zhao L, Wu X, Zuo B, Bian S, Li T, Liu X, Jiang Y, Chen C and Bi J 2024 *J. Mater. Chem. A* **12** 24041
[97] Choi I H, Jeong S G, Jeong D G, Seo A, Choi W S and Lee J S 2025 *Adv. Sci.* **12** 2407382
[98] Yang J, Daqiqshirazi M, Ritschel T, Bahrami A, Lehmann S, Wolf D, Feng W, Pöhl A, Charvot J and Bureš F 2024 *ACS Nano* **18** 17500
[99] Jeong S G, Seo A and Choi W S 2022 *Adv. Sci.* **9** 2103403
[100] Kwon H, Khan A I, Perez C, Asheghi M, Pop E and Goodson K E 2021 *Nano Lett.* **21** 5984
[101] Fu J, Huang J and Bernard F 2021 *Composites Communications* **28** 100917
[102] Xie G, Ding D and Zhang G 2018 *Adv. Phys. X* **3** 1480417
[103] Maranets T and Wang Y 2025 *Int. J. Therm. Sci.* **217** 110018
[104] Wu X, Wu Z, Liang T, Fan Z, Xu J, Nomura M and Ying P 2025 *Phys. Rev. B* **111** 085413
[105] Hu R and Tian Z 2021 *Phys. Rev. B* **103** 045304
[106] Wang J, Cao X H, Zeng Y J, Luo N N, Tang L M and Chen K Q 2023 *Appl. Surf. Sci.* **612** 155914
[107] Singh A K, Gao W and Deb P 2024 *ACS Appl. Mater. Interfaces* **16** 35438
[108] Lee S, Kim K, Kang D H, Meyyappan M and Baek C K 2019 *Nano Lett.* **19** 747
[109] Kang S, Lee K, Kim K, Jang J, Jung H, Jadhav B D, Son J S and Lee J E 2025 *Appl. Surf. Sci.* **692** 162733
[110] Shah S Z H, Aabdin Z, Tjiu W W, Nong W, Recatala-Gomez J, Chellappan V, Zhai W, Repaka D V M, Wu G and Hippalgaonkar K 2024 *ACS Appl. Mater. Interfaces* **16** 46191
[111] Heris H R, Kateb M, Erlingsson S I and Manolescu A 2022 *Surf. Interfaces* **30** 101834
[112] Li J, Tan Q, Li J F, Liu D W, Li F, Li Z Y, Zou M and Wang K 2013 *Adv. Funct. Mater.* **23** 4317
[113] Zheng W, Luo Y, Liu Y, Shi J, Xiong R and Wang Z 2019 *J. Phys. Chem. Lett.* **10** 4903
[114] Kim E B, Dharmaiah P, Lee K H, Lee C H, Lee J H, Yang J K, Jang D H, Kim D S and Hong S J 2019 *J. Alloys Compd.* **777** 703
[115] Kim M, Park D and Kim J 2024 *Ceram. Int.* **50** 3026
[116] Tanvir A N M, Bappy M O, Zeng M, Shang W, Wang K, Song K, Liu Y, Isotta E, Kanatzidis M G and Snyder G J 2024 *Energy Environ. Sci.* **17** 4560
[117] Zhou Z, Agne M T, Zhang Q, Wan S, Song Q, Xu Q, Lu X, Gu S, Fan Y and Jiang W 2019 *J. Materiomics* **5** 702
[118] Burton M, Howells G, Atoyo J and Carnie M 2022 *Adv. Mater.* **34** 2108183
[119] LeBlanc S, Yee S K, Scullin M L, Dames C and Goodson K E 2014 *Renewable and Sustainable Energy Reviews* **32** 313
[120] Li H, Chen C, Cheng J, Xia Y, Lyu S, Liu K, Xue W, Shen D, Wang W and Zhang Q 2025 *Nano Energy* **136** 110690
[121] Ming H, Luo Z Z, Zou Z and Kanatzidis M G 2025 *Chem. Rev.* **125** 3932